Sound generated in laminar flow past a two-dimensional rectangular cylinder

Y.S.K. Liow*, B.T. Tan, M.C. Thompson, K. Hourigan

*Fluids Laboratory for Aeronautical and Industrial Research (FLAIR), Department of Mechanical Engineering,
P.O. Box 31, Monash University, Victoria 3800, Australia*

Abstract

The far-field sound generated from low Mach number flow past a two-dimensional rectangular cylinder is studied by using a two-step aeroacoustic prediction method. In the first step, the incompressible Navier–Stokes equations are solved numerically. This allows the time-dependent acoustic source to be determined from Powell's vortex sound theory. Using this information, in the second step, the inhomogeneous wave equation is solved numerically to predict the time-evolving acoustic field. This study considers the effects of the Reynolds and Mach number on the sound generation and propagation characteristics. Results show that acoustic wave generation can be associated with the shedding of vortices at both the leading and trailing edges of the cylinder. In particular, an attempt is made to quantify the individual contributions, showing that the trailing-edge region is a considerably stronger source. Similar to the case for a circular cylinder, the predicted sound field has a dipolar far-field directivity with the lift dipole dominating. However, the drag dipole becomes relatively more important as the Reynolds number is increased. Overall, the relative amplitude of the far-field acoustic signal increases substantially with Reynolds number. In addition, as the Reynolds number is increased, the far-field pressure signal contains significant harmonic content, unlike the situation at the lowest Reynolds number investigated. A harmonic decomposition in terms of polar angle allows the multipole content of the signal to be quantified. Results showed that the acoustic field is dominated by the lift forcing which is predominantly dipolar, at least up to a Mach number (Ma) of 0.2. While this is also true for the drag forcing for low Mach numbers, we found that for $Ma > 0.1$, the quadrupole term is of a magnitude comparable to the drag dipole. By taking into account the Doppler effect through a spatial transformation of the predicted acoustic solution, the dipolar field becomes skewed towards the upstream direction as the Mach number is increased. Various difficulties associated with direct acoustic computations, such as convergence problems associated with initial transients and grid stretching, and the introduction of errors from under-resolving the acoustic source, and treatment of the slowly decaying wake, are discussed. The methods used to overcome these problems are reported.

1. Introduction

Flow past elongated bluff bodies has received much attention, numerically and experimentally, by a number of authors, for instance Parker and Welsh [1], Stokes and Welsh [2], Nakamura et al. [3], Hourigan et al. [4,5],

*Corresponding author. School of Engineering, Monash University Malaysia, P.O. Box 8975, Kelana Jaya, Selangor 46780, Malaysia. Tel.: +60 3 56360600; fax: +60 3 56329314.

E-mail address: keith.liow@eng.monash.edu.my (Y.S.K. Liow).

Naudasher and Wang [6], Mills et al. [7–9] and Tan [10]. The study of bluff body flows is important to fluid dynamicists as it underpins many engineering applications, e.g., aerodynamic loading of structures, flow-induced structural and acoustic vibration, mixing of fluids, and automobile aerodynamics. While extensive studies have been carried out on the bluff body flows, most of these were primarily focused on the dynamics of the instabilities. It is clear that we need to carry out more bluff body aeroacoustic research in order to develop further insight into the flow–acoustic interactions. In turn, this will enable us to develop more efficient noise prediction and attenuation techniques.

Historically, studies on the sound generated from flow past bluff bodies have focused on the circular cylinder. One of the earliest experiments on vortex-induced sound was conducted by Strouhal [11] who found that the frequency of the tone was identical to the vortex shedding frequency. This particular aeroacoustic phenomenon is also known as the Aeolian tone. Curle [12] has shown through analytical integration of Lighthill's [13] solution that the surface pressure fluctuations around the body lead to a dipole sound field. Previous investigators such as Gerrard [14], Phillips [15] and Etkin et al. [16], have experimentally confirmed that the Aeolian tone has a directivity normal to the fluid stream and is closely related to the lift force. Further insight into the Aeolian tones of a circular cylinder was provided by numerical simulations by many investigators, for instance Hardin and Lamdin [17], Cox et al. [18], Shen and Sorenson [19], Slimon et al. [20], and Inoue and Hatakeyama [21]. Most of the numerical studies just mentioned have considered the flow at a Reynolds number of 150–200 and a Mach number of $Ma = 0.2$.

In this study, Powell's [22] vortex sound theory is used in the computation of the acoustic radiation. Similar to other acoustic analogies, Powell's [22] vortex sound theory is based on the assumption that the acoustic lengthscale is much larger than the flow lengthscale. Because of this assumption, the energy levels of the sound field are also much smaller than that of the flow field. This implies that the sound field is decoupled from the flow field. Thus, there is no feedback from the aeroacoustic solution back to the aerodynamic solution. The far-field acoustic waves are generated by a localised source field which is limited to the regions of non-zero vorticity. Powell's [22] vortex sound theory has been used in various situations, mostly where the flow is both coherent and compact (e.g., Refs. [23–25]). Mitchell et al. [23] has compared the solution computed using Powell's vortex sound theory [22] with that of the DNS approach, and found good agreement. This confirms the validity of the former model when used in low Mach number flows.

The elongated bluff body, which forms the basis of this study, is a two-dimensional cylinder of rectangular cross section. The cylinder has square leading and trailing edges and is immersed in a fluid of uniform velocity. The dynamics of the flow are more complex relative to the circular cylinder because shedding occurs at both leading and trailing edges of the cylinder. The dynamics and acoustics of the vortex shedding from a rectangular cylinder are considered at two different Reynolds number of $Re = 300$ and 400. In terms of the wake dynamics, the boundary layers and vortices persist to higher Reynolds numbers even when the flow is turbulent (see Refs. [4,5]). Our focus in this study lies on the large-scale flow structures which contain much of the energy, and therefore, are responsible for the periodic sound generation. While it is possible to model a fully turbulent flow past a three-dimensional plate, it would certainly be very difficult to sort out the essential underlying physics behind the flow–acoustic interactions.

For both Reynolds numbers, the ratio of the cylinder chord to thickness is kept at $c/d = 7$. For a cylinder aspect ratio in the range of $3.2 < c/d < 7.6$, Parker and Welsh [1], Stokes and Welsh [2], and Tan [10] have found the presence of a regular vortex street in the wake with a distinct integer shedding mode of $n = 2$, i.e., there are two vortices originating from the leading edge distributed along both the upper and lower chords of the cylinder at any time. In this particular regime, both the leading- and trailing-edge shedding are strongly locked. The mechanism which controls the feedback loop between the leading- and trailing-edge shedding is known as an impinging leading edge vortex (ILEV) instability [6–9,26], or more recently proposed by Hourigan et al. [4,5] to be a combination of ILEV shedding and trailing edge vortex (TEV) shedding. Furthermore, the Strouhal number which is based on the cylinder thickness is approximately constant across the Reynolds number range simulated. Selection of this particular aspect ratio results in strong lock-in, e.g., the locking of the leading- and trailing-edge shedding to a single frequency and constant relative phase occurs rapidly. In addition, it is also relatively stable to perturbations [10,27]. This is advantageous from the acoustic perspective since the acoustic forcing is periodic and coherent. Furthermore, the frequency of the acoustic waves, which is identical to the lock-in frequency, is well defined.

The Reynolds number is based on the cylinder thickness. The values used in this study are $Re = 300$ and 400. These are chosen because previous flow studies by Sasaki and Kiya [28], and Tan et al. [27] have shown that at $Re = 400$, the flow is at the transition region from two- to three-dimensionality. Hence, at this particular Re range, we can treat the flow dynamics and acoustics as a purely two-dimensional problem. In turn, this allows us to focus our scope towards the roles of the periodic leading- and trailing-edge vortex structures on the sound generation without the added complications of phase variation along the span of the body, and turbulence in the flow. Furthermore, at this particular Re range, the predicted acoustic pressure field is expected to show similarities to that generated by flow past a circular cylinder at a comparable Reynolds number (see Ref. [21]). This is useful from our perspective, since it allows us to compare our results and findings with that of Inoue and Hatakeyama [21]. It should also be noted that the case of $Re = 300$ is designed to compare the different vortex structures and resulting differences in the acoustic properties. It is clear that the leading-edge shedding is significantly less vigorous, and the trailing-edge shedding is less compact and not as intense.

Fundamental acoustic modelling has been the main scope of investigation for many aeroacoustic workers, for example, the co-rotating vortex pair by Kambe and Minota [29], Mitchell et al. [23], Liow et al. [25], and the co-axial vortex ring pair by Tang and Ko [24], Verzicco et al. [30]. A cursory analysis of the flow specifications of the above-mentioned works and that of this study would reveal that the lengthscales are in the range of micro- to nanometres in air. With regard to physically realisable situations, such conditions would be relevant to engineering applications such as micro-vehicles and nano-machineries. Besides, the study is also relevant to flows on a macroscopic scale because as stated earlier, the large-scale flow structures formed are fairly insensitive to Reynolds number, and persist to higher Reynolds number. It is clear that fundamental acoustic research plays a major role in helping us gain insight into the flow–acoustic phenomena as well as developing better aeroacoustic prediction techniques. As mentioned earlier, one of the objectives of this study is to examine the roles played by the leading- and trailing-edge shedding on the sound radiation. As there is no external excitation, the shedding from the leading and trailing edge is natural. It is envisaged that the presence of the leading and trailing edges is associated with separate sound sources. In order to gain an insight into the flow–acoustic interactions, our analysis focuses on correlating the vorticity dynamics with the propagation characteristics of the acoustic waves. Finally, the effect of the Mach number on the propagation characteristics of the acoustic waves is also examined.

2. Numerical issues

In using Powell's [22] vortex sound theory to predict the far-field sound numerically, the computation of the acoustic solution is divided into two steps. In the first step, the time-dependent aerodynamic field is obtained through numerically solving the incompressible flow equations. The aerodynamic velocity field is then used to evaluate the acoustic forcing. In the second step, the acoustic pressure is obtained by numerically solving the inhomogeneous wave equation where the right-hand side term of the equation represents the acoustic forcing.

In contrast to the open-domain problem presented here, past studies have shown that there can be a strong back effect leading to the development of a resonant acoustic field when a rectangular cylinder is placed in a rigid walled duct. This is because, given the right conditions in a closed-domain problem, the acoustic field can modify the shear layers from both the leading and trailing edges, causing tight roll up of vortices periodically, thus leading to strong locking and reinforcement of the resonant field. However in this case, because of the open domain, it is clear that there is no chance for a resonant field to develop, i.e., there are no acoustic reflections from the external boundaries (both acoustic and aerodynamic).

While it is generally true that shear layers can be receptive to very low level external forcing, there is no need for explicit coupling in the problem presented here as the lock-in mechanism occurs independently of the Mach number. Here, the trailing-edge shedding, reinforced by the passing of leading-edge vortices over the trailing edge [4], leads to the modulation of the leading-edge shear layer, which controls subsequent leading-edge shedding and locks the flow (into the $n = 2$ mode). The control is through the hydrodynamic pressure field, since frequency stepping exists in both strictly incompressible flow simulations and slightly compressible experiments. As such, no explicit coupling is required for this problem. Of course, as the Mach number

approaches unity, the distinction between the aerodynamic (near) field and the aeroacoustic (far) field disappears, as does the appropriateness of this type of decoupled approach.

In theory, the acoustic field could modify the flow field through reflections of sound waves from boundaries, and perhaps through a direct modulation of the leading-edge shear layer. However, given the relatively small length scale near the plate when compared with the sound waves, the fluid flow and pressure fluctuations off the cylinder surface are well approximated by the assumption of flow incompressibility. Relative to the cylinder dimensions, the difference between an acoustic wavelength and an infinite one (at the limits of $Ma = 0$) would be negligible.

Difficulties aside, the two-step approach enables each of the solvers to be optimised for the coupled solution procedure for the flow and acoustic fields, which are governed by different length and velocity scales. As a result, the computational costs of the two-step approach can be significantly less than for direct simulation of the compressible flow fields.

The field of computational aeroacoustics (CAA) is unique and distinct from that of computational fluid dynamics (CFD) because of the different characteristics and requirements of the solution procedure. These issues have been discussed in great detail by, amongst others, Crighton [31], Tam [32], and Wells and Renaut [33]. In general, the primary objective of CAA is to accurately predict the acoustic solution associated with an unsteady flow field. In addition to the standard requirements of high spatial and temporal resolution, it is also important to take great care with the introduction of the acoustic source, with implementation of boundary conditions, to limit the spatial extent of the source, and to make the grid stretching sufficiently gentle. Attention to these factors is required to ensure that the predicted acoustic field does not become contaminated with spurious noise. These factors have been successfully addressed in the earlier case study to predict the acoustic radiation from an isolated co-rotating vortex pair [25]. The details are provided in the next section.

3. Methodology

3.1. Flow modelling issues

In the present study, the fluid is assumed to be Newtonian and (almost) incompressible. As such, it is governed by the Navier–Stokes equations and the incompressibility constraint

$$\frac{\partial \mathbf{u}}{\partial t} = -(\mathbf{u} \cdot \nabla)\mathbf{u} - \nabla p + \frac{1}{Re}\nabla^2 \mathbf{u}, \tag{1}$$

$$\nabla \cdot \mathbf{u} = 0. \tag{2}$$

Here, the flow velocity is $\mathbf{u}$, and p is the kinematic pressure. The incompressible flow equations are solved using the CFD software package, FLUENT, which is a finite-volume solver. The spatial and temporal discretisations used by the CFD solver are second-order accurate. A schematic of the flow configuration is shown in Fig. 1. The cylinder centroid is fixed at $(0,0)$. The ratio of the cylinder chord, c, to thickness, d, is $c/d = 7$. This particular aspect ratio is selected in order to produce a strong lock-in in the $n = 2$ shedding regime. (This means that the vortex structure from leading-edge shedding arrives at the trailing edge one full shedding period later, so that there are two vortices between the leading and trailing edge at any time on either
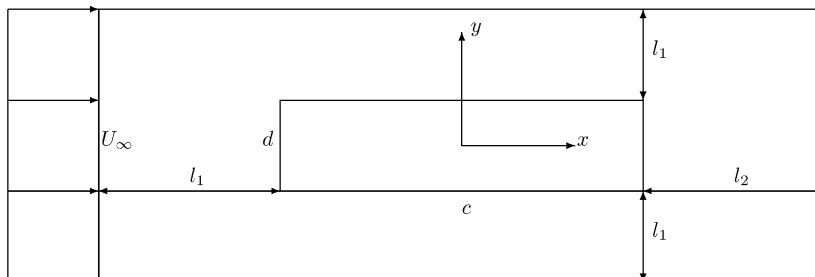
Fig. 1. Schematic of flow past a long rectangular cylinder. Note that the sketch is not to scale.

side of the cylinder.) The direction of the freestream velocity U_∞ is from left to right. Here, the Reynolds number, based on the freestream velocity U_∞ and the cylinder thickness d, is defined as $Re \equiv \rho_0 U_\infty d / \mu$. The Strouhal number St, again based on the cylinder thickness, is defined as $St \equiv fd/U_\infty$, where f is the shedding frequency. The Mach number is based on the wave propagation speed c_0 and is defined as $Ma \equiv U_\infty/c_0$.

At the cylinder surface, the no-slip velocity condition was imposed. The freestream velocity was enforced at the top and bottom computational boundaries. In compressible computations, the 'buffer zone' approach is used in order to allow both vortex structures and sound waves to pass freely without causing significant reflections back into the domain. However, in the present simulations, the flow is assumed to be incompressible and backflow is not expected. As such, the outflow boundary condition used in our simulations only need to allow vortex structures to pass. Hence, the pressure boundary condition was imposed at the outflow. This forces the pressure to be a constant and the velocity components to have zero normal gradient. The main issue then is the distance of the outflow boundary away from the trailing face of the plate. A domain independence study has been conducted to ensure that the outflow boundary is placed sufficiently far so that the main flow features around the plate are not significantly affected.

The size of the CFD domain is defined by the three parameters, l_1, l_2 and l_3 as shown in Fig. 1. The computational domain is discretised into a structured mesh of $N_x \times N_y$ grid points as shown in Fig. 2(a). In order to ensure that the physics of the flow is modelled to within acceptable accuracy limits, a domain independence test followed by spatial and temporal resolution tests were carried out. The vorticity around the trailing edge was used to monitor the solution convergence. It was decided that a maximum pointwise error of 5% was adequate for the current study. The distances from the cylinder to the artificial computational boundaries have to be selected carefully to reduce blockage effects (e.g., see Ref. [34]). Three different values for the normal length as measured from the cylinder boundaries to the external boundaries (except for the downstream length) were tested, i.e., $l_1/d = 10, 15$ and 20. After the value for l_1/d has been determined, the appropriate value for the downstream length is tested, i.e., $l_2/d = 15, 30, 45$. Once the domain size has been established, the grid spacing was tested with $\Delta x/d = 0.0125, 0.02$ and 0.04. It is clear that the minimum grid spacing at the cylinder surface has to be sufficiently small to resolve the velocity gradients in the boundary layers. In addition, the effect of the geometrical singularities at each of the four sharp corners of the cylinder can be minimised through the use of a fine grid spacing. Finally, the temporal resolution study consisted of running simulations with different timesteps: $\Delta t U_\infty/d = 0.1, 0.2$ and 0.4. As a result of these extensive tests, the computational parameters for the flow simulation were chosen as follow; $l_1 = 15d$, $l_2 = 45d$, Δx (and Δy) $= 0.025d$, and $\Delta t = 0.01d/U_\infty$.

3.2. Acoustic modelling issues

According to Powell [22], the governing equation for the far-field acoustic pressure is

$$\frac{\partial^2 p}{\partial t^2} - c_0^2 \nabla^2 p = \nabla \cdot (\boldsymbol{\omega} \times \mathbf{u}), \tag{3}$$

where p is the normalised acoustic pressure, and $\boldsymbol{\omega}$ is the vorticity vector. For the two-dimensional case, ω is the only non-zero vorticity component, and lies in the spanwise direction. We will refer to the above equation as the acoustic wave equation, which is solved using the finite-difference method. The spatial terms are discretised using sixth-order finite-differences derived from Taylor series expansions at neighbouring points. A central-difference stencil is used in the discretisation scheme for numerical stability and accuracy. The acoustic wave equation is advanced temporally using a fourth-order Runge–Kutta scheme. Such high-order methods are needed to minimise dispersion and dissipation errors.

A reflecting boundary condition is implemented on the cylinder surfaces. The radiation boundary condition that is based on the approach taken by Bayliss and Turkel [35], is used in most linear acoustic wave modelling applications. Therefore it is applied at the external boundaries. Since the dominant acoustic source region is located mainly in the vicinity of the cylinder and decays rapidly away from it, the governing inhomogeneous wave equation effectively reverts to the homogeneous wave equation in the far field. Therefore, the issue of acoustic sources associates with the Powell [22] source term, $\nabla \cdot (\omega \times \mathbf{V})$, passing through the external
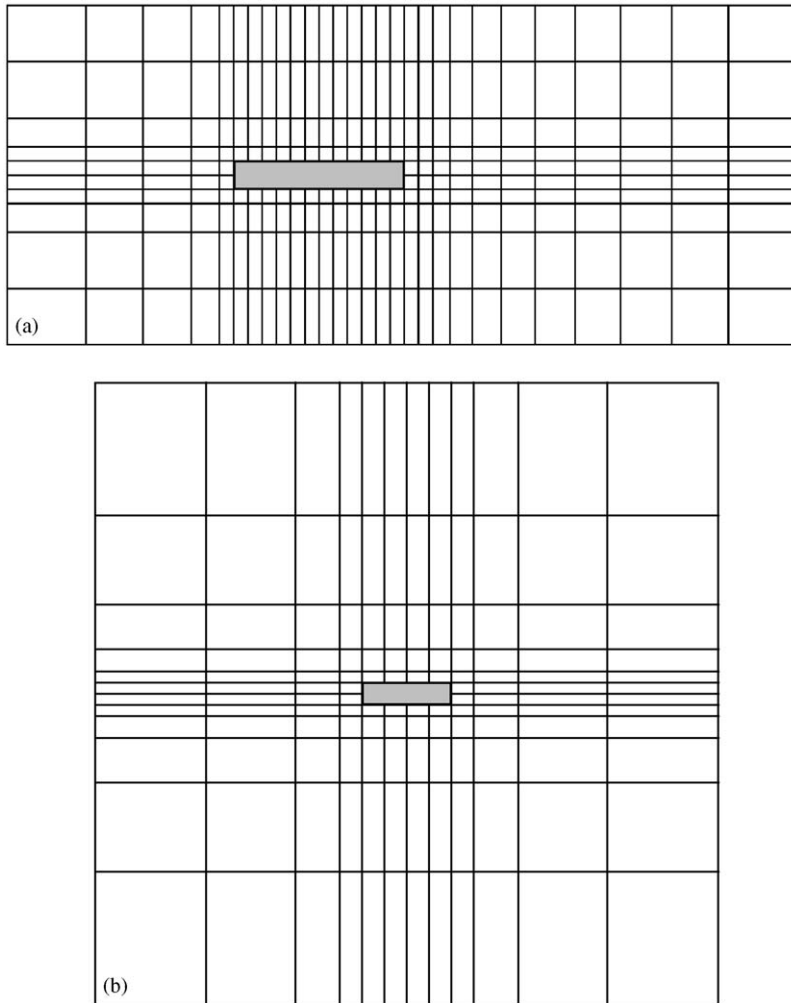
Fig. 2. Typical meshes used in the respective (a) flow, and (b) acoustic simulations. Note that the size of the CFD and CAA meshes are not to scale.

boundaries does not occur. Direct application of the central sixth-order spatial scheme to points adjacent to the boundaries would reference points external to the domain. To avoid this and to maintain accuracy, a set of one-sided difference stencils that maintain sixth-order accuracy are used when evaluating the spatial derivatives at those points.

The CAA domain covers two acoustic wavelengths in the positive and negative x and y directions. This is sufficient to capture the propagation and decay of the waves. Similar to the CFD domain, the CAA domain is discretised into a structured mesh of N_a^2 grid points. Here the subscript a is used to define the CAA parameters to avoid confusion with the CFD parameters. However, the grid in the acoustic simulation is arranged differently to the CFD grid. A typical grid used in the acoustic simulations is shown in Fig. 2(b). The near-field grid spacing is identical to that of the CFD grid while the far-field grid spacing is such that there is a minimum of 20 points across an acoustic wavelength. The grid stretching ratio, $(\Delta x_{i+1}/\Delta x_i)_a$, has to be not too far from unity to allow acoustic waves to propagate freely without generating spurious reflections and noise as they pass through the stretched grid region. The choice of the stretching ratio (1.03) was validated for the lowest Mach number studied and was subsequently fixed for the remaining acoustic simulations. As a result, the CAA domain size and total number of grid points varied according to Mach number.

Owing to the fact that the grid point distributions in the CFD and CAA domains are different, it is necessary to interpolate the hydrodynamic velocity field from the CFD domain to the CAA domain so that the acoustic source can be evaluated. Two-dimensional second-order interpolation, using the closest CFD mesh points, allowed the spatial accuracy of the CFD solution to be maintained during this transfer process. This was set up efficiently through a *mapping* matrix, which stored the set of interpolation points and the corresponding weighting coefficients for each CAA grid point. The velocity components, (u_a, v_a), on the acoustic grid are then obtained directly from a matrix–vector multiply at any given time.

When evaluating the acoustic forcing field on the CAA mesh, it is essential that the hydrodynamic field is fully resolved, even away from the hypothesised acoustic source regions [36]. The acoustic source depends on the second derivative of the velocity field so small errors in the flow field calculation can lead to large errors in the acoustic source. In addition, for practical flows, the spatial decay back to the freestream condition is slow, and the CFD domain has a limited size often with reduced resolution towards the outer boundaries. To overcome this problem, spatial windowing is applied to reduce the computed acoustic source smoothly to zero away from true source region(s). Unlike the flow case here, the application of a spatial window in a compact flow is relatively simple because there is no extensive wake region [25]. Curle [12] has predicted that at low Mach numbers, the wake from bluff body flows gives rise to a distribution of quadrupoles. Quadrupoles are a less efficient source than dipoles (which arise from surface pressure fluctuations around the body). As such, removing part of the wake is not expected to substantially affect the far-field acoustic signal.

In the application of the spatial window, the velocity components in the acoustic domain are multiplied by spatial functions f_x and f_y as follows:

$$u'_a = u_a \times f_x f_y + (U_\infty - f_x f_y), \tag{4}$$

$$v'_a = v_a \times f_x f_y. \tag{5}$$

The spatial functions f_x and f_y are unity close to the cylinder and decay smoothly to zero away from the cylinder surfaces. The windowing is controlled by the two decay lengths, l_{b1} and l_{b2}, as shown in Fig. 3. To verify that the spatial window prevents the generation of spurious noise but does not unduly affect the acoustic predictions, the lengths, l_{b1} and l_{b2}, are tested over a wide range. It was expected that the predicted acoustic field would not be sensitive to the window length scale, l_{b1}, which controls windowing upstream, and above and below the cylinder chord. This proved to be the case and this decay length was chosen as $l_{b1} = 3d$ for the remainder of the simulations. The downstream decay length scale has a stronger effect on the predictions since wake vortices pass through the windowing region. Acoustic predictions using different values for l_{b2} were compared. The predicted far-field acoustic field was essentially invariant for $l_{b2} \geqslant 30d$, and hence $l_{b2} = 35d$ was chosen for the majority of the simulations. While it is necessary to have spatial windowing in order to obtain a smooth and non-spurious acoustic solution, its application at the downstream region also serves to prevent the outflow boundary condition used in the flow simulation from becoming an artificial acoustic source term. This is because the wake vortices exiting the outflow CFD boundary would become a source term if interpolated from the flow domain into the acoustic domain. In direct simulations, a 'sponge region' is incorporated into the outflow boundary condition to prevent the large-scale flow structures exiting the boundary from generating spurious noise (see Ref. [37]).

The acoustic forcing of Powell [22] derived from the instantaneous hydrodynamic field obtained from the flow simulations cannot be used directly in the acoustic wave equation, or at least, it is preferable not to do so.
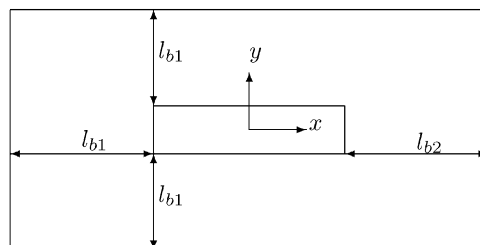
Fig. 3. Schematic showing the spatial window decay lengths used in the CAA modelling. The sketch is not to scale.

This is because the hydrodynamic field contains a fluctuating component as well as a time-invariant component. If the acoustic simulation is undertaken using the acoustic forcing as it is, the acoustic field would most likely be dominated by the time-mean component which can mask the fluctuating component. Since the time-invariant component does not contain any temporal information, it should be removed prior to evolving the acoustic solution. This is achieved by subtracting the time-mean acoustic source from the original acoustic source. The time-mean is obtained by averaging the source over an acoustic cycle.

One common source of spurious noise is from the crude implementation of initial conditions leading to the generation of large-amplitude initial transients. These can propagate through the domain and, where they pass through the stretched grid, are almost certain to lead to the generation of spurious high-frequency waves. Because these unphysical waves travel in all directions, they contaminate the near-field as well as the far field. One solution is to allow the acoustic forcing to be ramped up gradually. This step is implemented through multiplication of the acoustic forcing with a temporal ramping function, f_t, at every time step over a period t_r. The function f_t is zero at initialisation and increases gradually and smoothly to unity over the period t_r. After considerable testing, we found that $t_r = 3.5d/U_\infty$ was sufficient to restrict the amplitude and increase the timescale of the initial transient to be comparable to those of the real acoustic waves. This is sufficient to prevent contamination of solution as the transient propagates through the stretched grid and passes through the radiation boundary.

The temporal ramping and spatial window functions were chosen to be quintic polynomials with the coefficients determined by enforcing continuity of the function, and the first and second derivatives, at both ends of the ramping or windowing domains.

4. Results and discussion

In this section, the results of the flow simulations are presented and analysed to gain an understanding into the vorticity dynamics. This is followed by the presentation of the acoustic predictions and then an analysis of the flow–acoustic interactions. Note that in the following sections, all lengths have been normalised by cylinder thickness, d, and times by d/U_∞. In addition, the symbol t^* denotes the retarded time.

4.1. Flow dynamics

Flow simulations are performed on a rectangular cylinder of aspect-ratio $c/d = 7$ at Reynolds numbers of $Re = 300$ and 400. Prior to the evolving the flow, the velocity field over the entire CFD domain was initialised with the freestream velocity U_∞. The flow took approximately 80–100 time units to start developing an asymmetric pattern at the edges of the cylinder. The simulation then took a further 100 time units (about 20 cycles) for the shedding of vortices to become fully periodic. To monitor the flow state, a time trace of the base pressure coefficient, C_p, starting from the non-dimensional time of 250 time units is shown in Fig. 4. The measurement of the base pressure was taken at the centre of the trailing face. It is clear from the figure that the flow has reached a periodic asymptotic state. Furthermore, the mean and standard deviation of C_p increase with Reynolds number. As the base pressure cofficient is closely related to the overall drag, this implies that the amplitude of the fluctuating drag force also increases with Reynolds number. The shedding frequency is estimated by using the time histories of the C_p signal. The period of C_p is half that of the shedding period because the base pressure coefficient is measured at the centre of the trailing face. From Table 1, it is clear that there is little variation in the Strouhal number (based on cylinder thickness) between Reynolds numbers. This implies that at both Reynolds numbers, the instability belongs to the same shedding mode. The flow dynamics are revealed through a series of vorticity snapshots over one shedding cycle in Figs. 5 and 6. At each Reynolds number, the first vorticity plot in the sequence is taken at approximately the same phase of the shedding cycle. The figures show that the shedding mode in both cases corresponds to the $n = 2$ shedding mode. The figures also reveal that vortex shedding at the trailing edge occurs between leading-edge vortices passing the trailing edge. Away from the cylinder, the leading- and trailing-edge vortices form a combined wake vortex which then convects at an approximately constant convective velocity. The phase of the leading- and trailing-edge shedding appears to be approximately the same for the two Reynolds numbers simulated.
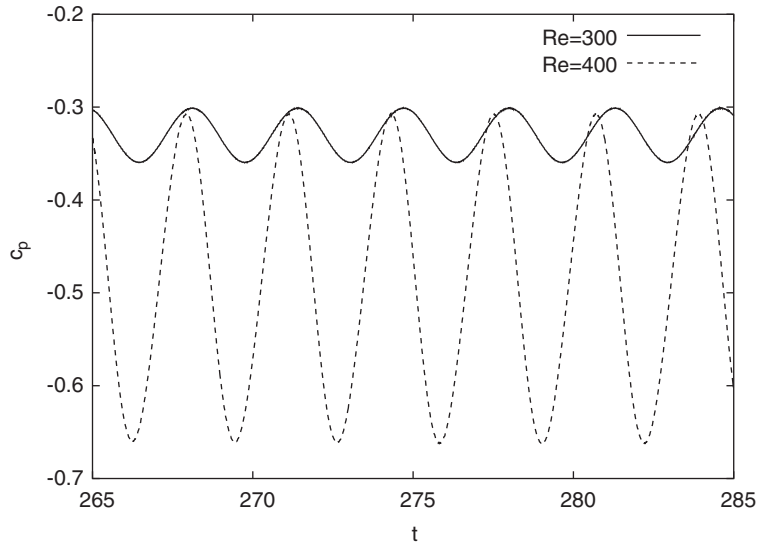
Fig. 4. A sample trace of 25 time units of the base pressure recorded at the centre of the trailing face.

Table 1
Strouhal number based on thickness, mean base pressure coefficient and mean drag coefficient for the two Reynolds numbers simulated

Re	c/d	St	$\bar{c}_p$	$\bar{c}_d$
300	7	0.152	−0.332	0.864
400	7	0.156	−0.483	1.005

Tan et al. [27] have found that strong lock-in and high base suction occurs when the leading-edge vortex does not reach the trailing edge until the trailing-edge vortex has had time to develop first. Furthermore, this phasing varies a little as the aspect ratio is increased, until a switch occurs to a new shedding mode. Another point of interest is that the leading- and trailing-edge shedding are much more well defined at the higher Reynolds number. Specifically, the vortices along the cylinder chord are stronger and more concentrated.

Figs. 7 and 8 show instantaneous snapshots of the Powell [22] acoustic source field at quarter period intervals, corresponding to the times shown in Figs. 5 and 6. These fields are complex and difficult to interpret. They consist of various regions, such as the boundary layers at the top and bottom of the cylinder and the wake region, in which the localised source merely convects downstream with little change in form. At the trailing-edge, the source field undergoes considerable variation throughout the cycle, and this is presumably the main source region. At the higher Reynolds number, the source variation is stronger due to the more compact vortex structures from both the leading and trailing edges.

4.2. Lift and drag forces

The time histories of the lift coefficient, C_l, and drag coefficient, C_d, are shown in Fig. 9. Similar to C_p, the periodic nature of the lift and drag traces at both Reynolds numbers indicate that the flow is strongly locked to the $n = 2$ shedding mode. As expected, the mean lift coefficient is zero because the cylinder geometry is symmetric about the x-axis. The standard deviation of the lift coefficient is used in further analysis. The increase in the magnitude of the fluctuating lift force at the higher Reynolds number is attributed
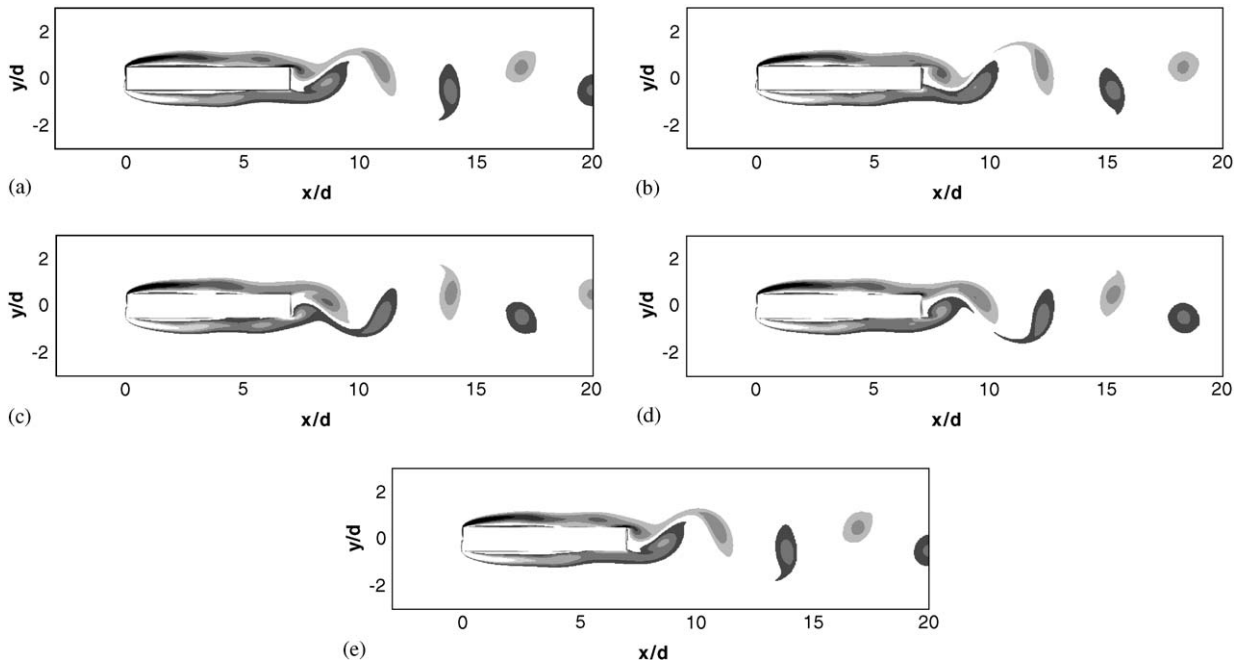
Fig. 5. Snapshots of instantaneous vorticity showing the time development of the flow structure around the rectangular cylinder at $Re = 300$. The simulation times correspond to (a) $t = 253$, (b) $t = 254.5$, (c) $t = 256.3$, (d) $t = 257.8$, (e) $t = 259.6$. The range of the contour levels is $\omega = \pm 3.8$ with 11 increments. Vorticity has been non-dimensionalised with respect to U_∞ and d. A reverse color map is used for the negative vorticity.
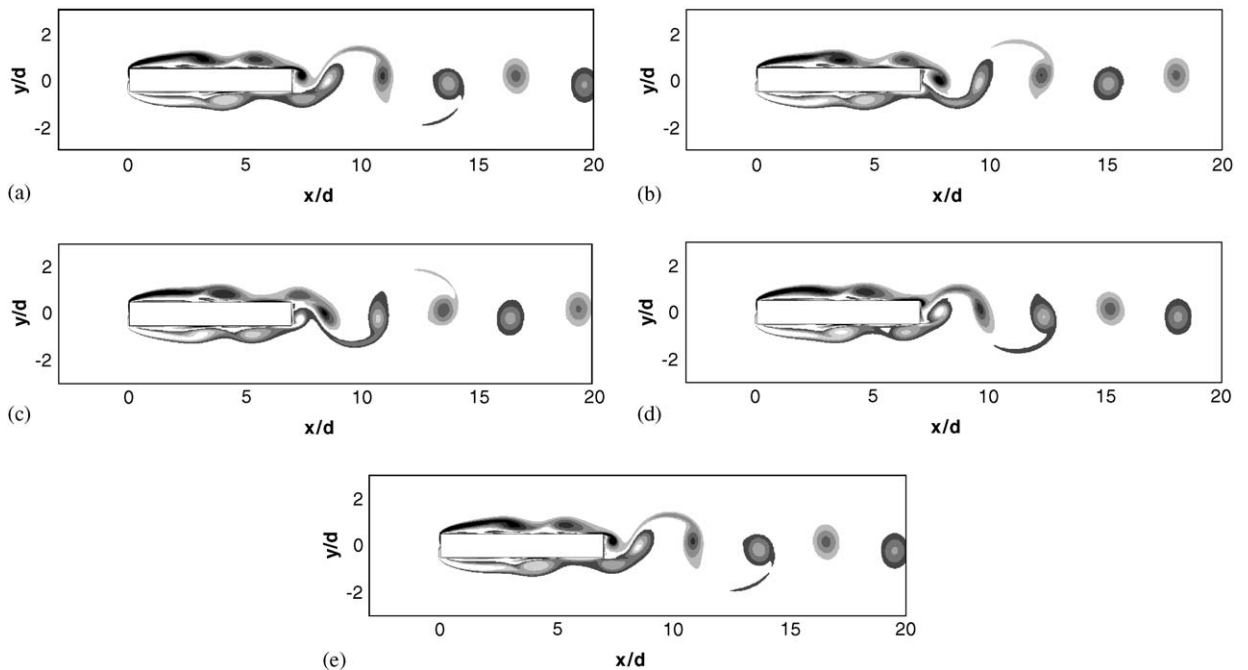
Fig. 6. Snapshots of instantaneous vorticity showing the time development of the flow structure around the cylinder at $Re = 400$. The simulation times correspond to (a) $t = 250.4$, (b) $t = 251.9$, (c) $t = 253.4$, (d) $t = 255.2$, (e) $t = 256.7$. The range of the contour levels is the same as that of Fig. 5.
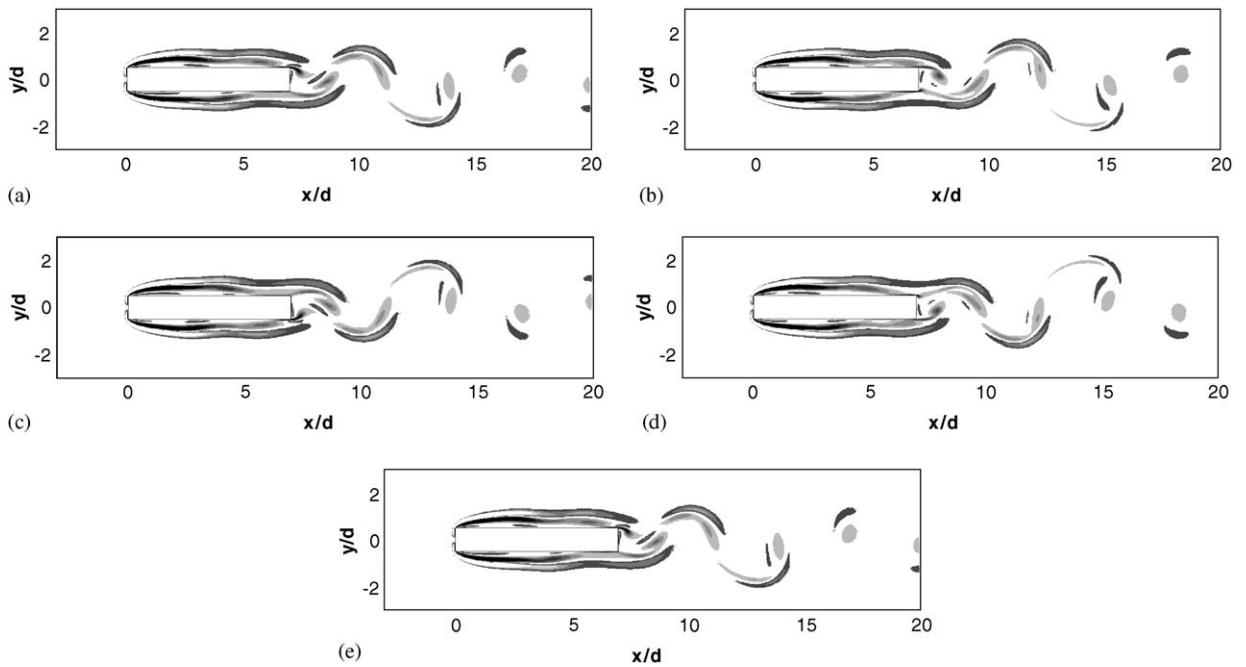
Fig. 7. Snapshots showing contours of the instantaneous acoustic source at quarter period intervals for $Re = 300$. The time frames correspond to those of Fig. 5. The range of the contour levels is $\nabla \cdot (\omega \times \mathbf{v}) = \pm 10$ with 11 increments. The source term has been non-dimensionalised with respect to U_∞ and d.
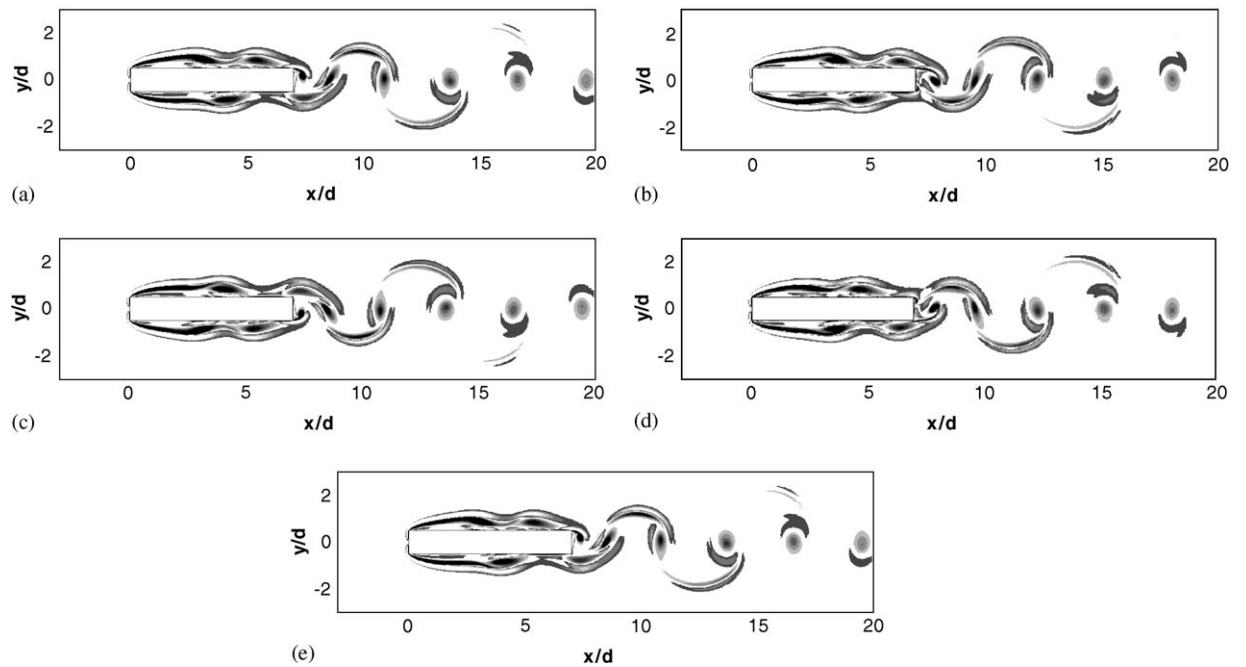
Fig. 8. Snapshots showing contours of the instantaneous acoustic source at quarter period intervals for $Re = 400$. The time frames correspond to those of Fig. 6. The range of the contour levels is the same as that of Fig. 7.

to the more intense vortex structures forming at the edges of the cylinder. In contrast, the contributions to the lift force from the vortices convecting along the top and bottom chords of the cylinder approximately cancel each other out.
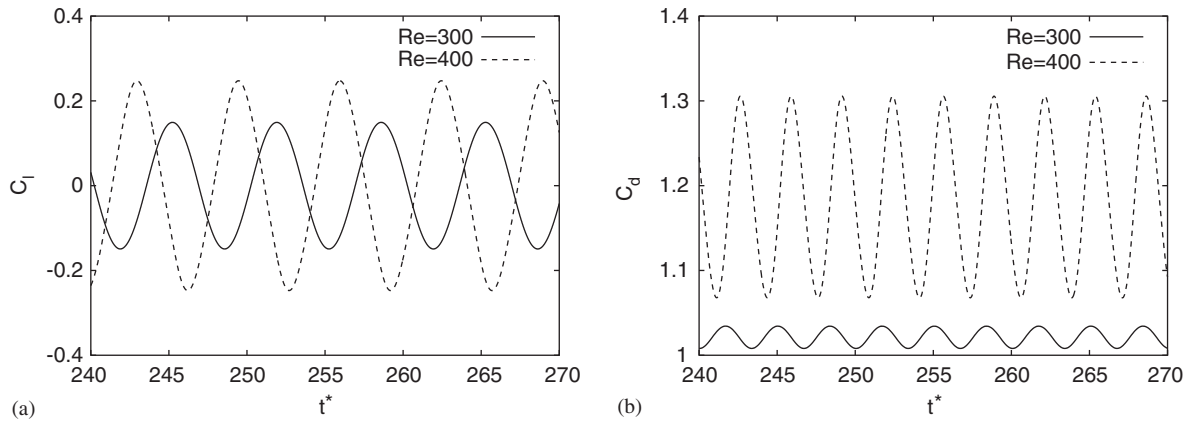
Fig. 9. A representative time trace of: (a) lift coefficient C_l, and (b) drag coefficient C_d, at the two Reynolds numbers simulated.

Fig. 9 also shows that the standard deviation of C_l is much greater than that of C_d. From Etkin et al. [16] argument that the strength of the acoustic signal is proportional to the magnitude of the fluctuating force, this suggests that in these acoustic simulations, the lift dipole should be more significant than the drag dipole. After comparing the magnitude of the fluctuations in C_l and C_d over the simulated Reynolds number range, both the lift dipole and drag dipole are expected to be more intense at $Re = 400$. This is because both fluctuating components of C_l and C_d increase with Reynolds number. While Inoue and Hatakeyama [21] have shown that the acoustic generation mechanism is independent of the Mach number over the restricted range $Ma = 0.05$–0.2, they have not considered Reynolds number dependence. Our results of this study indicate that the source mechanism is indeed significantly influenced by the Reynolds number.

4.3. Propagation and decay of acoustic waves

At each Reynolds number, acoustic simulations are performed at three different Mach numbers: $Ma = 0.05$, 0.1 and 0.2. While the flow simulations were started from a stationary state, the acoustic computations are only initiated after the flow has reached a fully periodic state. The flow simulation has effectively reached its periodic asymptotic state after a non-dimensional time of approximately 250 units. The acoustic field was then evolved for a further 25 time units. This corresponds to approximately four shedding cycles.

The time histories of the acoustic pressure at the far-field observation positions of $(r, \lambda) = (\lambda/2, \pm 90°)$ are shown in Fig. 10. Here, r is the polar radial coordinate and the angle θ is measured anticlockwise from the x-axis. These observation points, placed at a radial distance of half an acoustic wavelength from the cylinder centroid, are representative of the far-field acoustic behaviour. Further monitoring positions at $r = \lambda$ and 2λ showed virtually identical functional variation. At the selected angles of $\theta = \pm 90°$, the amplitude of the fluctuations in the acoustic pressure is maximal in accordance with the direction of the lift force. From Fig. 8, the acoustic signal at $\theta = 90$ was found to be $180°$ out-of-phase with that at $\theta = -90°$. This is expected because the shedding of the leading- and trailing-edge vortices is symmetric about the x axis but shedding from the top surface is $180°$ out of phase from that from the bottom surface. The frequency of the acoustic oscillations matches the shedding frequency verifying that the acoustic signals are locked to the shedding. For each Reynolds number, when the Mach number is reduced by a factor of two, the amplitude of the signal drops by approximately one order of magnitude. At a particular Mach number, the amplitude of the sound signal increases with Reynolds number, which implies the strength of the acoustic source increases with Reynolds number, at least over the restricted Reynolds number range considered.

To investigate the relative phasing between the lift force, shedding of the leading- and trailing-edge vortices, and the acoustic signal, time histories of the aerodynamic forces, shedding cycle, and the acoustic signal are correlated. It is clear from Figs. 10 and 11 that the negative peaks of the fluctuations in C_l correspond to the positive peaks of p at $\theta = 90°$ and negative peaks of p at $\theta = -90°$. Conversely, when
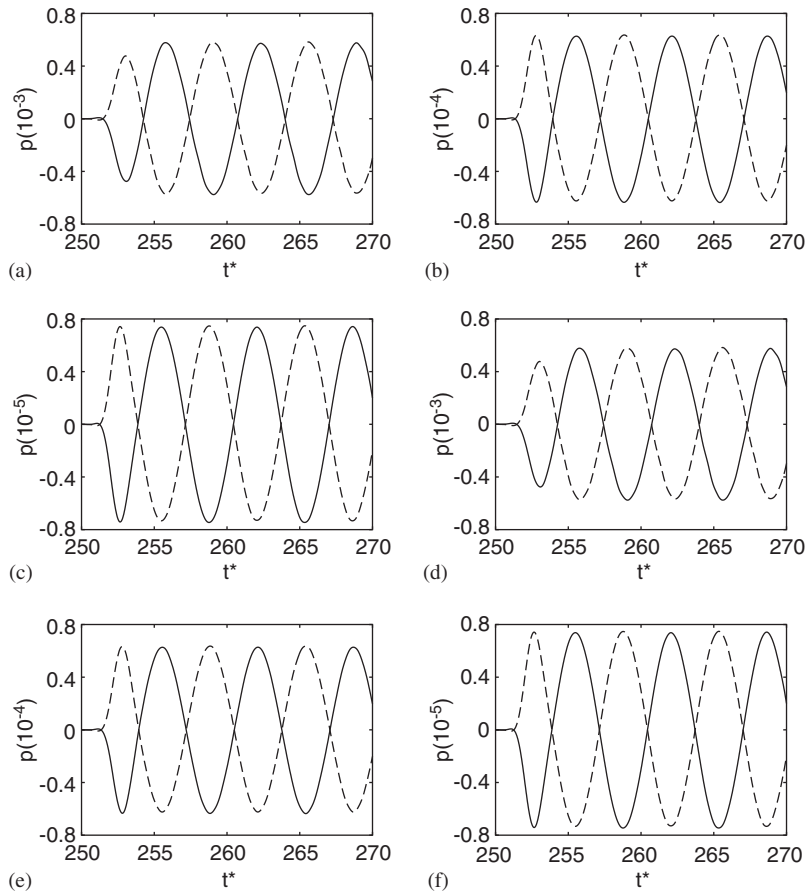
Fig. 10. Time histories of acoustic pressure fluctuations at $(r,\theta) = (\lambda/2, \pm 90°)$ for the three Mach numbers. Here, $Ma = 0.2$ for (a) and (d); $Ma = 0.1$ for (b) and (e); and $Ma = 0.05$ for (c) and (f). The left column shows results for $Re = 300$ and results for $Re = 400$ are shown at the right. Note that the solid lines represents $90°$ while the dashed line represents $-90°$.
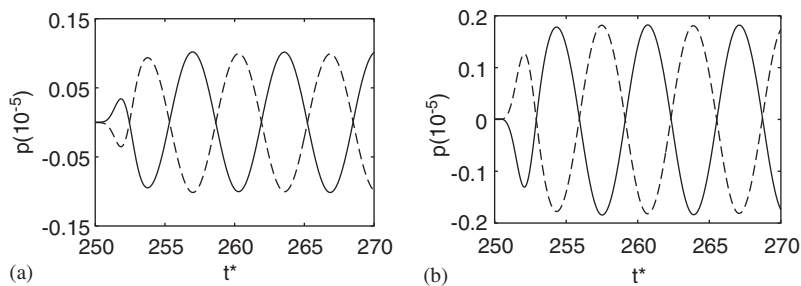
Fig. 11. Time histories of acoustic pressure fluctuations at $(r,\theta) = (\lambda/2, \pm 90°)$ for $Ma = 0.05$. Here, only the leading-edge region is involved as both the trailing edge, and wake regions are effectively removed using the spatial window. Note that the solid line represents $90°$ while the dashed line represents $-90°$.

the C_l has a positive peak, the acoustic signal has a positive peak at $\theta = -90°$ and a negative peak at $\theta = 90°$. Furthermore, the positive acoustic peaks at $90°$ and negative acoustic peaks at $-90°$ occurred at approximately the instant when the leading- and trailing-edge vortices are beginning to shed from the lower trailing edge. Consequently, at the instant where shedding occurs at the upper trailing edge, the acoustic peak is positive at $-90°$, and negative at $90°$.

Instantaneous contours of the acoustic pressure field at a selected simulation time of $t = 274$ are shown in Figs. 12 and 13. Several interesting features can be drawn out, first by observing the pressure contours, and then by comparing those with the vorticity dynamics occurring at the same times. It is clear that over the Reynolds and Mach number range considered in this study, the acoustic radiation is largely dominated by the lift dipole. The drag dipole is virtually absent as it is at least one order of magnitude smaller than the lift dipole. Consistent with the lift fluctuations, the acoustic signal radiated in the y direction is 180° out of phase with that radiated in the $-y$ direction. While both simulations show strong similarities in the lift dipole dominance, there is one significant difference. At the former Reynolds number, the sound field is virtually symmetric about the y-axis for all three Mach numbers while this is certainly not the case for the latter. This suggests that at the former Reynolds number, the far-field directivity is largely caused by the shedding of the vortices at the trailing edge, and less by the leading edge shedding and vortices moving along the top and bottom side of the cylinder. In contrast, at $Re = 400$, the sound field is noticeably less symmetrical about the y-axis as the wave propagation angle deviates from 90°. This deviation is most likely caused by the better defined leading edge shedding, and more compact and concentrated vortices forming at the top and bottom sides of the cylinder. We also found a correlation between the far-field directivity with the shedding of the trailing edge vortices, i.e., the propagation direction is greater than 90° when the trailing edge vortex is being shed at the bottom side of the cylinder. The opposite holds when the shedding of the trailing edge vortex occurs at the top side of the cylinder. These observations imply that the acoustic generation mechanism in a rectangular cylinder is much more complex than that of a circular cylinder at similar Reynolds and Mach numbers.

Inoue and Hatakeyama [21] have argued that the alternate shedding of vortices into the wake is the source of the acoustic waves generated from laminar flow past a two-dimensional circular cylinder. Furthermore, the generation mechanism is described in terms of acoustic pressure pulses of equal strength but 180° out-of-phase. However, the time traces of the acoustic pressure were sinusoidal. At the lower Reynolds number of
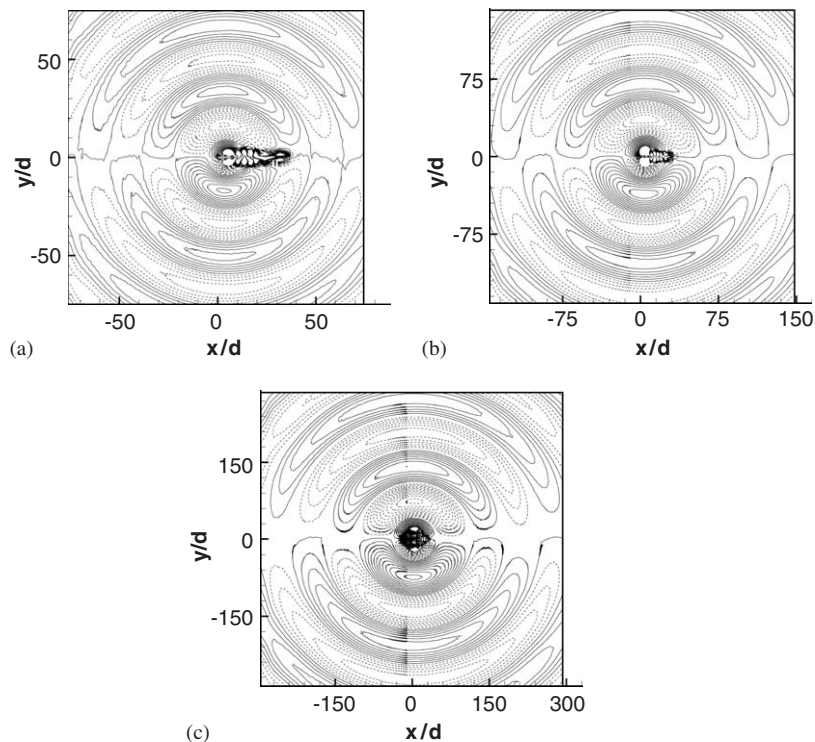
Fig. 12. Contours of the acoustic pressure at a particular time instant of $t^* = 275$ for $Re = 300$. The Mach numbers are: (a) $Ma = 0.2$; (b) $Ma = 0.1$; (c) $Ma = 0.05$. The pressure contour levels are: (a) $\pm 9.5 \times 10^{-4}$; (b) $\pm 9.5 \times 10^{-5}$; (c) $\pm 9.5 \times 10^{-6}$ with 31 increments.
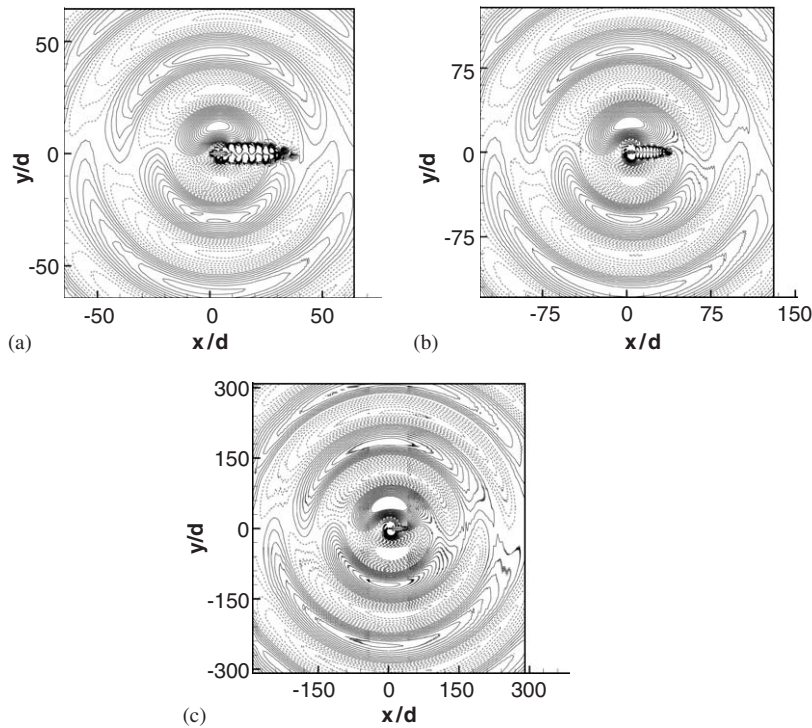
Fig. 13. Contours of the acoustic pressure at a particular time instant of $t^* = 275$ for $Re = 400$. The Mach numbers are: (a) $Ma = 0.2$; (b) $Ma = 0.1$; (c) $Ma = 0.05$. The pressure contour levels are: (a) $\pm 1 \times 10^{-3}$; (b) $\pm 1 \times 10^{-4}$; (c) $\pm 1 \times 10^{-5}$ with 31 increments.

$Re = 300$ the results of the current study show good agreement with those of Inoue and Hatakeyama [21]. This suggests that at $Re = 300$, the acoustic waves generated from the leading- and trailing-edge regions combine to form a sinusoidal signal. However at $Re = 400$, the traces of the acoustic pressure show a significant departure from being purely sinusoidal. To be able to associate characteristics of the signal with a particular region, the leading- and trailing-edge source regions have to be isolated before the acoustic field is evolved. Since the leading- and trailing-edge shedding are in-phase and locked, the components of the acoustic field associated with the leading- and trailing-edge regions should complement each other. To predict the acoustic signal generated solely from the leading-edge region, the spatial windowing of the wake is extended upstream so that it effectively removes the sources associated with the trailing-edge region as well as the wake. Truncating the source over part of the cylinder chord may seem undesirable; however, contributions to the lift force from vortices convecting along the top and bottom surfaces of the cylinder chord effectively cancel each other. The exact x location of the truncation position along the chord was varied between $x_{cent} \pm 1$, where x_{cent} is the cylinder centroid, to test the effect. This showed only slight variations in the phase and amplitude of the far-field signal, confirming the applicability of the approach.

The acoustic signals computed only with the leading-edge source region active are shown in Fig. 11. There are two interesting points to note. First, the amplitude of the acoustic signals are considerably smaller. This suggests that the dominant sound source is associated with the trailing-edge region. Second, for both Reynolds numbers, the acoustic signals are clearly sinusoidal, implying that the leading-edge shedding is effectively producing sinusoidal waves over the Reynolds number range studied. This further suggests that acoustic waves generated from the trailing-edge region assume a less sinusoidal state as the Reynolds number is increased from $Re = 300$ to 400, or that the two regions combine with a phase difference to produce the effect. As the Reynolds number is increased, the leading-edge vortices are more compact as they pass the trailing edge, as are trailing-edge vortices as they form and shed from the trailing edge. Thus, it is perhaps not surprising that the trailing-edge source becomes less sinusoidal as the Reynolds number increases.

4.4. Decomposition of the pressure field

In classical acoustic analysis, the acoustic field is frequently depicted mathematically as point sources resulting in monopole-, dipole- or quadrupole-type far-field radiation patterns. Here, we perform a spatial decomposition of our predicted acoustic pressure field into a sum of multipoles. This allows us to quantify the different modes present in the acoustic field. By comparing the relative amplitudes of the different modes, we can easily determine the dominant mode present in the field. Furthermore, the effect of changing Mach number on the relative amplitudes of the harmonic modes can be considered. Generalisation of the acoustic field as a linear sum of harmonic functions is possible owing to the linearity of the acoustic waves. The expansion used by Inoue and Hatakeyama [21] is adopted in the present study and is given by

$$p(r, \theta) = A_0(r) + \sum_{m=1} B_m(r) \sin(m\theta) + \sum_{m=1} C_m(r) \cos(m\theta), \tag{6}$$

where $m = 1, 2, \ldots \infty$. The symbol A_0 represents the monopole, while B_1 and C_1 are dipoles associated with the fluctuations in the lift and drag forces, respectively. Furthermore, as the integer m increases, the corresponding higher-order terms associated with B_m and C_m correspond to sine and cosine multipoles of order m. At a fixed radial position, these terms can be evaluated from the expressions:

$$A_0(r) = \frac{\pi}{2} \int_0^{2\pi} p(r, \theta) \, d\theta,$$

$$B_m(r) = \frac{1}{\pi} \int_0^{2\pi} p(r, \theta) \sin(m\theta) \, d\theta,$$

$$C_m(r) = \frac{1}{\pi} \int_0^{2\pi} p(r, \theta) \cos(m\theta) \, d\theta. \tag{7}$$

In this study, the above-mentioned integrals were evaluated through integration of the predicted pressure field. The numerical scheme of Simpson's $\frac{1}{3}$ rule was used. At the selected radial location, a total of 5000 data points evenly spaced over 360° was used for the integration. The integrands at the data points were interpolated from the Cartesian acoustic grid using second-order polynomial interpolation.

Time histories of the dipoles and quadrupoles (calculated at the polar radial location of $r = \lambda/2$) are shown in Figs. 14 and 15. The figures show that at both Reynolds numbers, the lift dipole dominates all other terms irrespective of Mach number. The drag dipole C_1 was found to be at least one order of magnitude smaller than that of the lift dipole. Thus, the sound field is mostly a result of the fluctuating lift rather than the fluctuating drag for both Reynolds numbers studied. This is in good agreement with Inoue and Hatakeyama [21]. As expected, the difference in the time histories of the lift dipoles and pressure fluctuations decreases with decreasing Mach number, and the lift dipole overlaps the pressure fluctuations at $Ma = 0.05$. The difference is thought to be caused by the sine quadrupole B_2 which was found to be the second most dominant harmonic term. As the Mach number is increased, the relative amplitude ratio of B_2/B_1 also increased, indicating that the deviation in the wave propagation angle (from 90°) increases with Mach number. One possible explanation is that as the Mach number becomes larger, the flow structure around the plate can no longer be viewed as a pure mathematical point source. Rather, it would consist of multiple sources radiating waves from their respective spatial locations. It is also clear that the amplitude of the lift dipole increases with Reynolds number. This is expected since the lift coefficient increases with Reynolds number (see Fig. 9).

Another interesting feature is that the drag dipole is not the dominant component amongst the cosine modes for the higher Mach numbers of $Ma = 0.1$ and 0.2. Thus, while the lift dipole dominates over the Mach number range studied, there appears to be no distinctly dominant cosine mode (associated with the drag force) for a Mach number greater than 0.05. This may have also been caused by the non-compactness of the drag source structure.
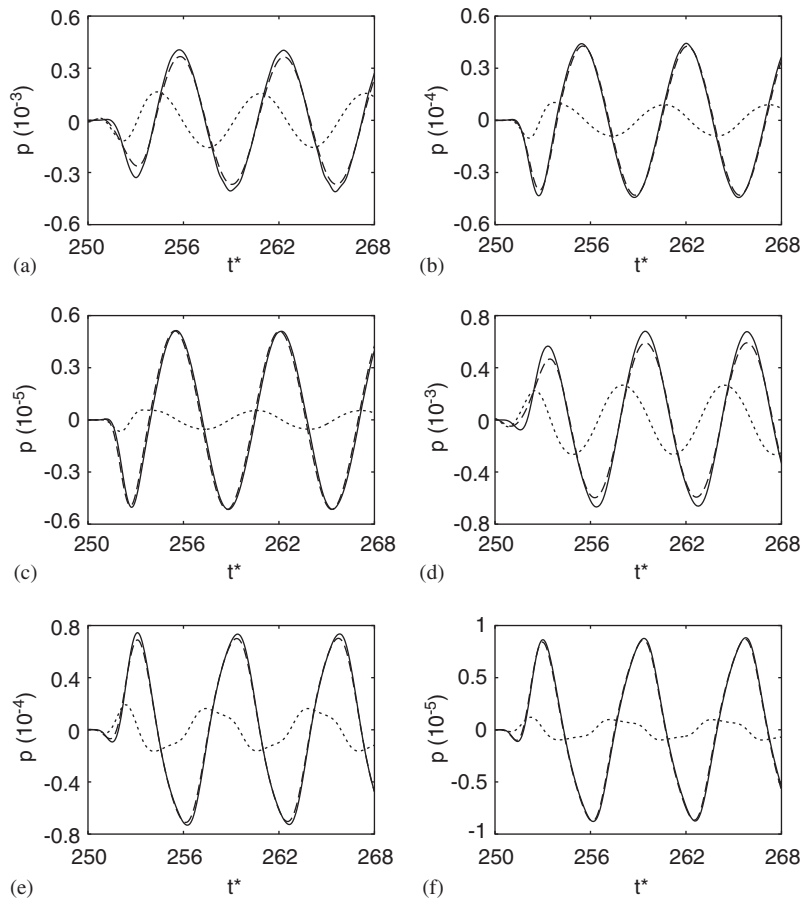
Fig. 14. Time histories of the sine modes at $Re = 300$ (left) and $Re = 400$ (right). The modes are calculated at the radial distance of $r = \lambda/2$. Here, $Ma = 0.2$ for (a) and (d); $Ma = 0.1$ for (b) and (e); and $Ma = 0.05$ for (c) and (f). Solid line represents pressure fluctuations, dashed line represents lift dipole, and dotted line represents $\sin(2\theta)$ quadrupole.

4.5. The effect of the Mach number

In Powell's [22] theory of vortex sound, the acoustic medium is assumed to be at rest. The acoustic wave equation does not explicitly include the convective term (and this is actually beneficial when interpreting the acoustic field in terms of multipoles). Inoue and Hatakeyama [21] have found from their study that while the Mach number does not have any effect on the generation mechanism, the directivity of the acoustic field is greatly influenced by finite Mach number. This effect is due to a Doppler shift. Since the background flow velocity merely adds vectorially to the acoustic velocity, this effect can be included through postprocessing of the predicted acoustic solution. It involves a transformation of the spatial positions of the acoustic waves at any given time in the domain as follows:

$$r' = \frac{r}{1 - Ma \cos \theta}, \tag{8}$$

where r' is the Doppler-shifted radial position. Note that this transformation is valid for small Mach numbers only.

The instantaneous contours of the Doppler-shifted pressure field at a non-dimensional time of $t^* = 275$ are shown in Figs. 16 and 17. The deviation of the acoustic wave propagation angle from $90°$ of the (dipolar)
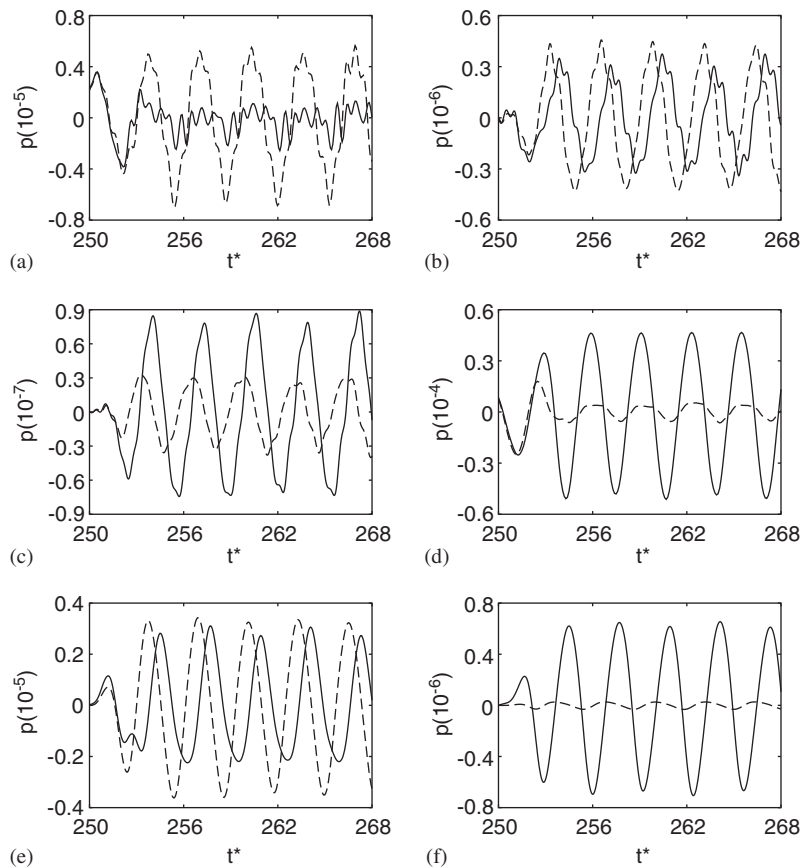
Fig. 15. Time histories of the cosine modes at $Re = 300$ (left) and $Re = 400$ (right). The modes are calculated at the radial distance of $r = \lambda/2$. Here, $Ma = 0.2$ for (a) and (d); $Ma = 0.1$ for (b) and (e); and $Ma = 0.05$ for (c) and (f). Solid line represents drag dipole, dashed line represents $\cos(2\theta)$ quadrupole.

acoustic field when the Doppler effect is included is clearly seen when the pressure contours are compared to those without the Doppler shift. As found by Inoue and Hayakeyama [21], the Doppler shift causes a skewing of the dominantly dipolar field towards the upstream direction. This effect, while clearly seen at $Ma = 0.2$, becomes less significant as the Mach number is decreased. The upstream skewing decreases with Mach number, and the wave propagation angle almost reverts to $90°$ at $Ma = 0.05$.

5. Conclusions

The results from a numerical investigation into the acoustic radiation from laminar flow past a two-dimensional cylinder of rectangular cross section are presented in this study. A two-step aeroacoustic prediction method was used where the incompressible flow equations were first solved numerically followed by computation of the time-evolving acoustic field by directly solving the acoustic wave equation. This study expands on the many previous investigations of acoustic radiation from flows past bluff bodies. In particular, the results can be compared with those for flow past a two-dimensional circular cylinder. The more complex geometry of a rectangular cylinder leads to vortex shedding from both the leading and trailing edges, and in turn these regions may be considered to be localised acoustic sources. As such, the roles of the leading- and trailing-edge shedding on acoustic radiation is considered with particular attention to the effects of Reynolds number, albeit for only a restricted range.
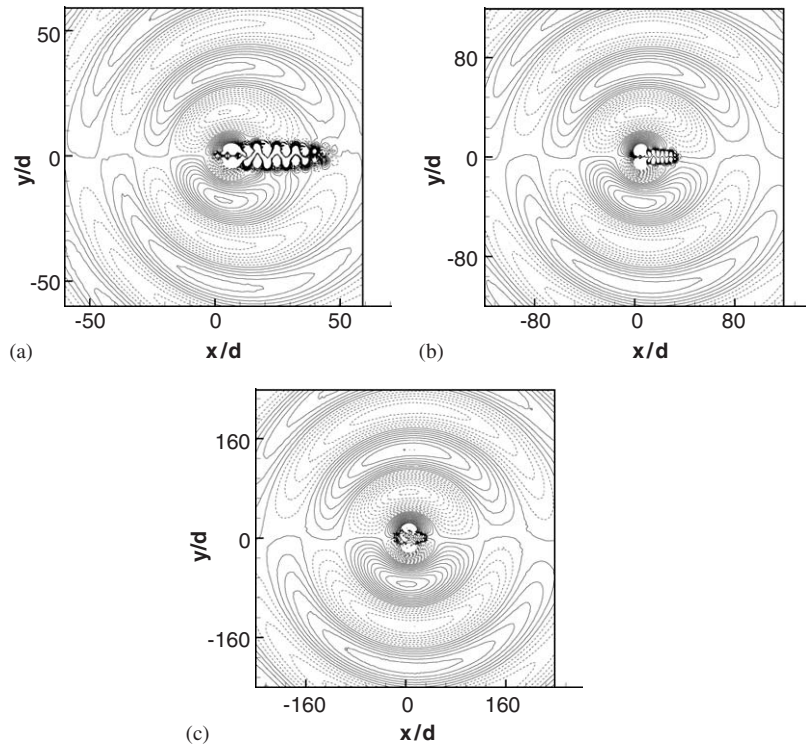
Fig. 16. Contours of the Doppler-shifted acoustic pressure at a particular time instant of $t^* = 275$ at $Re = 300$. The Mach numbers are: $Ma = 0.2$ for (a); $Ma = 0.1$ for (b); and $Ma = 0.05$ for (c). The contour levels are the same as in Fig. 12.

Computations of the acoustic field at two different Reynolds numbers of $Re = 300$ and 400 produced far-field pressure distributions similar to those observed for a circular cylinder but with some distinct differences. The lift dipole clearly dominated the drag dipole by at least one order of magnitude. At Mach numbers above $Ma = 0.05$, an azimuthal Fourier expansion showed that the multipole field associated with drag fluctuations was not dominated by the dipole term at $r = \lambda/2$. This is likely to be due to the non-compactness of the source. Over the Mach number range simulated, varying the decay length of the window function in the wake, indicated that away from the body the wake was not a significant sound source. This is consistent with the accepted view that pairs of wake vortices from opposite side of the wake can be associated with acoustic sources which effectively cancel each other out. In turn, this enforces the view that sound waves actually radiate from the region close to the cylinder. For the present geometry, the leading- and trailing-edge regions effectively give rise to separate sound sources. Because the leading- and trailing-edge shedding are strongly locked for the selected cylinder aspect ratio, the two sound sources complement each other and are in phase. Furthermore, at $Re = 300$, the acoustic waves from the leading- and trailing-edge regions are approximately sinusoidal and lead to a far-field acoustic field which oscillates sinusoidally. However, at $Re = 400$, the acoustic signal is less sinusoidal. The non-sinusoidal nature of the far-field oscillation is probably associated with the more complex trailing-edge source in this case, consisting of compact forming and shedding vortices at the trailing edge, and compact leading-edge vortices passing the trailing edge at times in between. Isolation of the leading-edge source showed that region led to a sinusoidal far-field oscillation at both Reynolds numbers.

While Powell's [22] vortex sound theory assumes that the acoustic medium is at rest, the convective effect of non-zero Mach numbers (also known as the Doppler shift) can be incorporated into the predicted acoustic solution in a postprocessing step. This involves a spatial transformation of the radial position to take into account the effect of the freestream velocity as well as the wave propagation speed. Consistent with Inoue and
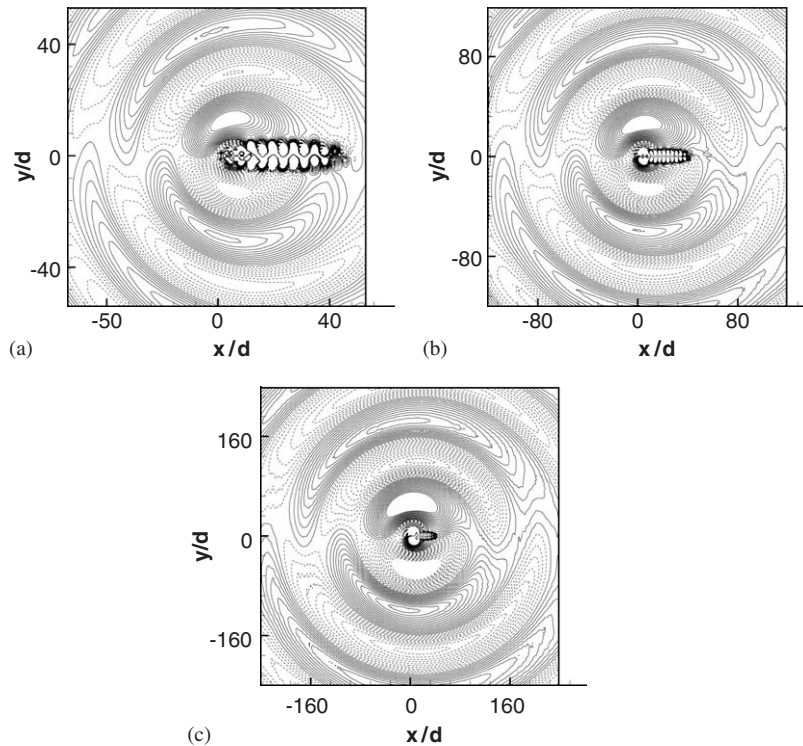
Fig. 17. Contours of the Doppler-shifted acoustic pressure at a particular time instant of $t^* = 275$ at $Re = 400$. The Mach numbers are: $Ma = 0.2$ for (a); $Ma = 0.1$ for (b); and $Ma = 0.05$ for (c). The contour levels are the same as in Fig. 13.

Hatakeyama's [21] results, the wave propagation angle was found to tend towards the upstream direction resulting in a skewing of the dipolar sound field when the Mach number was increased.

Acknowledgements

References

[1] R. Parker, M.C. Welsh, Effects of sound on flow separation from blunt flat plates, *International Journal of Heat and Fluid Flow* 4 (1983) 113–127.

[2] A.N. Stokes, M.C. Welsh, Flow-resonant sound interaction in a duct containing a plate II: square leading edge, *Journal of Sound and Vibration* 104 (1986) 55–73.

[3] Y. Nakamura, Y. Ohya, H. Tsuruta, Experiments on vortex shedding from flat plates with square leading and trailing edges, *Journal of Fluid Mechanics* 222 (1991) 437–447.

[4] K. Hourigan, R. Mills, M.C. Thompson, J. Sheridan, P. Dilin, M.C. Welsh, Base pressure coefficients for flows around rectangular plates, *Journal of Wind Engineering and Industrial Aerodynamics* 49 (1993) 311–318.

[5] K. Hourigan, M.C. Thompson, B.T. Tan, Self-sustained oscillations in flows around long flat plates, *Journal of Fluids Structure* 15 (2001) 387–398.

[6] E. Naudasher, Y. Wang, Flow-induced vibrations of prismatic bodies and grids of prisms, *Journal of Fluids and Structure* 7 (1993) 341–373.

[7] R.H. Mills, J. Sheridan, K. Hourigan, M.C. Welsh, The mechanism controlling vortex shedding from rectangular bluff bodies, in: R.W. Bilger (Ed.), *12th Australasian Fluid Mechanics Conference*, Sydney, Australia 10–15 December, 1995, pp. 227–230.

[8] R. Mills, J. Sheridan, K. Hourigan, Response of base suction and vortex shedding from rectangular prisms to transverse forcing, *Journal of Fluid Mechanics* 461 (2002) 25–49.

[9] R. Mills, J. Sheridan, K. Hourigan, PIV and flow visualisation of flow around rectangular cylinders, *Journal of Fluid Mechanics* 478 (2003) 299–323.

[10] B.T. Tan, Vortex Shedding and Interactions in Flows around Bluff Plates, PhD Thesis, Department of Mechanical Engineering, Monash University, Melbourne, Australia, 2000.

[11] V. Strouhal, Ueber eine besondere art der tonerregung, *Annual Review of Physics and Chemistry (New Series)* 5 (1878) 216–251.

[12] N. Curle, The influence of solid boundaries upon aerodynamic sound, *Proceedings on Royal Society of London A* 231 (1955) 505–514.

[13] M.J. Lighthill, On sound generated aerodynamically: I. General theory, *Proceedings of Royal Society, London A* 221 (1952) 564–587.

[14] J.H. Gerrard, Measurements of the sound from circular cylinders in an air stream, *Proceedings of the Physical Society London, Section B* 68 (1955) 453–461.

[15] O.M. Phillips, The intensity of aeolian tones, *Journal of Fluid Mechanics* 1 (1956) 607–624.

[16] B. Etkin, G.K. Korbacher, R.T. Keefe, Acoustic radiation from a circular cylinder in a finite stream (aeolian tones), *Journal of the Acoustical Society of America* 29 (1957) 30–36.

[17] J.C. Hardin, S.L. Lamdin, Aeroacoustic computation of cylinder wake flow, *AIAA Journal* 22 (1984) 51–57.

[18] J.S. Cox, K.S. Brentner, C.L. Rumsey, Computation of vortex shedding and radiated sound for a circular cylinder: subcritical to transonic Reynolds number, *Theoretical and Computational Fluid Dynamics* 12 (1998) 233–253.

[19] W.Z. Shen, J.N. Sorenson, Comment on the aeroacoustic formulation of Hardin and Pope, *AIAA Journal* 37 (1999) 141–143.

[20] S.A. Slimon, M.C. Soteriou, D.W. Davis, Computational aeroacoustics simulations using the expansion about incompressible flow approach, *AIAA Journal* 37 (1999) 409–416.

[21] O. Inoue, N. Hatakeyama, Sound generation by a two-dimensional circular cylinder in a uniform flow, *Journal of Fluid Mechanics* 471 (2002) 285–314.

[22] A. Powell, Theory of vortex sound, *Journal of the Acoustical Society of America* 36 (1) (1967) 177–195.

[23] B.E. Mitchell, S.K. Lele, P. Moin, Direct computation of the sound from a compressible co-rotating vortex pair, *Journal of Fluid Mechanics* 285 (1994) 181–202.

[24] S.K. Tang, N.W.M. Ko, On sound generated from the interaction of two coaxial vortex rings moving in the same direction, *Journal of Sound and Vibration* 187 (2) (1995) 287–310.

[25] Y.S.K. Liow, M.C. Thompson, K. Hourigan, Computation of acoustic waves generated by a co-rotating vortex pair, in: B.B. Dally (Ed.), *14th Australasian Fluid Mechanics Conference*, Adelaide, Australia, 9–14 December, 2001, pp. 99–102.

[26] E. Naudasher, D. Rockwell, *Flow-Induced Vibrations: An Engineering Guide*, A.A. Balkema, Rotterdam, Brookfield, 1994.

[27] B.T. Tan, M.C. Thompson, K. Hourigan, Simulation of perturbed flow around a rectangular cylinder, in: *Proceedings of the ASME Fluids Engineering Division Summer Meeting*, Washington, DC, USA, 21–25 June, 1998.

[28] K. Sasaki, M. Kiya, Three-dimensional vortex structure in a leading-edge separation bubble at moderate Reynolds number, *Journal of Fluids Engineering* 113 (1991) 405–410.

[29] T. Kambe, T. Minota, Sound radiation from vortex system, *Journal of Fluid Mechanics* 74 (1) (1981) 61–72.

[30] R. Verzicco, A. Iafrati, G. Riccardi, M. Fatica, Analysis of the sound generated by the pairing of two axisymmetri co-rotating vortex rings, *Journal of Sound and Vibration* 200 (3) (1997) 347–358.

[31] D.G. Crighton, Computational aeroacoustics for low Mach number flows, in: J.C. Hardin, M.Y. Hussaini (Eds.), *Computational Acoustics*, Springer, New York, 1992, pp. 50–68.

[32] C.K.W. Tam, Computational aeroacoustics: issues and methods, *AIAA Journal* 33 (10) (1995) 1788–1796.

[33] V.L. Wells, R.A. Renaut, Computing aerodynamically generated noise, *Annual Review of Fluid Mechanics* 29 (1997) 161–199.

[34] D. Barkley, R.D. Henderson, Three dimensional Floquet stability analysis of the wake of a circular cylinder, *Journal of Fluid Mechancis* 322 (1996) 215–241.

[35] A. Bayliss, E. Turkel, Radiation boundary condition for wave-like equations, *Communication on Pure and Applied Mathematics* XXXIII (1980) 707–725.

[36] S.C. Crow, Aerodynamic sound emission as a singular perturbation problem, *Studies in Applied Mathematics* XLIX (1) (1970) 21–44.

[37] T. Colonius, S.K. Lele, P. Moin, Sound generation in a mixing layer, *Journal of Fluid Mechanics* 330 (1994) 375–409.